Depth-sensing indentation at macroscopic dimensions

Jeremy Thurn[a] Dylan J. Morris, and Robert F. Cook
Department of Chemical Engineering and Materials Science, University of Minnesota, Minneapolis, Minnesota 55455

(Received 4 June 2002; accepted 27 July 2002)

A macroscopic-scale depth-sensing indentation apparatus with the ability to be mounted on an inverted microscope for *in situ* observation of contact events was calibrated using the Oliver and Pharr [J. Mater. Res. **7,** 1564 (1992)] procedure with a two-parameter area function. The calibrated Vickers tip was used to determine the projected contact area at peak load and the modulus and hardness of a variety of non-metallic materials through deconvolution of the measured load-displacement traces. The predicted contact area was found to be identical to the measured area of residual contact impressions. Furthermore, for transparent ceramic materials the projected contact area during loading was found to be the same as the area measured from the diagonal of post-indentation residual contact impressions. The modulus and hardness values deconvoluted from the load–displacement traces were compared with independent measurements. The effects of sample clamping, column compliance, and tip radius on the load–displacement data and inferred materials properties were also examined. It is suggested that the simplicity of instrumentation and operation, combined with the ability to observe indentations optically, even *in situ,* makes macroscopic-scale depth-sensing indentation ideal for fundamental studies of contact mechanics.

I. INTRODUCTION

A. Motivation

Depth-sensing indentation (DSI) has in recent years become a common technique for characterization of metals,[1] ceramics,[2] and polymers.[3] In particular, small-load indentations are being used to characterize thin film and surface layer properties[4] and small-scale deformation phenomena.[5] Analysis of the load–displacement (*P-h*) data recorded continuously throughout the load–unload cycle provides information about the projected contact area at peak load, which is coupled with the measured unloading stiffness to provide estimates of the elastic modulus and hardness. The analysis method, however, requires careful calibration to determine the column compliance and indenter tip shape. The most popular calibration technique is that of Oliver and Pharr,[6] which is based on the elastic solution of Sneddon[7] for indentation by an axisymmetric body. It is the purpose of this work to examine this calibration technique at large loads and macroscopic length scales at which the indentation impressions can be examined optically. The calibration and analysis procedures of Oliver and Pharr are used to examine a variety of nonmetallic materials with a two-parameter area function introduced previously.[8] The indentation impression area, elastic modulus, and hardness are determined from the *P-h* traces, and the areas are compared with those determined from direct optical measurements of the residual indentation impression. The post-indentation corner-to-corner area is shown to be equivalent to the contacted indentation area at peak load for three transparent ceramics by mounting the indenter on an inverted microscope and observing the contact event *in situ*. Further, the effects of column compliance, clamping of the sample, and indenter tip radius on the *P-h* traces and the properties extracted from them are examined. The loading traces are examined for applicability of geometric similarity, and the unloading traces are examined for applicability of the Oliver and Pharr power-law analysis.

DSI at macroscopic length scales has been performed on many custom-built[2,9–20] and commercial devices (such as the Instron MicroTester, Instron Corp., Canton, MA, and the Zwick ZHU, Zwick GmbH & Co., Ulm, Germany) and has numerous advantages. The most obvious is the ability to observe the indentation contact area and any related cracking directly, both *in situ* and post-indentation, by optical microscopy.[11] This will be taken

[a]Present address: Seagate Technology, Bloomington, Minnesota 55435

advantage of in this work in an effort to validate the commonly used deconvolution technique of Oliver and Pharr[6] to determine the impression area from the *P-h* trace. The ability to observe crack initiation and growth during the indentation cycle at loads typical for indentation toughness measurements was taken advantage of in a similar instrument by Cook and Pharr[13] to provide valuable insight into the fracture behavior of ceramic materials. DSI at these loads can also be used to provide an estimate of the displaced volume driving crack growth during unloading, a parameter that is lumped into a material-independent constant in the relationship for indentation toughness[21] and indentation delamination models for thick films.[11,22] Simultaneously, DSI at macroscopic length scales can be used to determine the modulus and hardness of the materials for use in the same models. In fact, it can be used to characterize the modulus and hardness of thick films and coatings in much the same manner that nanoindentation is commonly used to examine thin films. The time-dependent properties of soft viscoelastic and viscoelastoplastic materials and coatings can be probed with relaxation tests as most macroscopic DSI devices operate under direct displacement-control (i.e., there are no feedback loops that complicate creep and relaxation tests on commercial instruments). Direct control over the displacement rate also makes the device easier in general to control and build, while the macroscopic scale of the device makes it easier and cheaper to build. Similarly, the indenter tips are much larger than for nanoindentation and are significantly less expensive to purchase in a variety of shapes. While nanoindentation is incredibly important for deducing the elastic and plastic properties of thin films, macroscopic-scale DSI is more advantageous for the study of the mechanics of contact (especially during the contact event) and the fracture and delamination resulting from the indentation event.

B. *P-h* relationships during loading and unloading

Indentation hardness H has been defined as

$$H = \frac{P_{\max}}{A} \quad , \tag{1}$$

where $P_{\max}$ is the peak indentation load and A is the projected contact area at peak load. Figure 1 is a representative load–displacement trace (on soda-lime glass) showing $P_{\max}$ and other variables used in this analysis. Figure 2 is a schematic cross-section of the indentation process showing the contact dimension a (a is the contact radius for conical indentation and half the contact diagonal for Vickers indentation), the total displacement h, the contact displacement h_c, and included angle of the indenter 2α. For conical indenters, $A = \pi a^2$ and for Vickers indenters $A = 2a^2$. For metals and most ceramic materials, the indentation impression diagonals measured following the indentation event are assumed to be the same as those at peak load, as inferred from experimental investigations of Vickers indentation (both diagonals),[23] Knoop indentation (the long diagonal only),[24] and roller indentation with "blunt" rollers (the track width).[25] The projected contact area at peak load can thus be related to the indentation contact depth by simple geometrical arguments. For a conical indenter, $A = \pi \tan^2 \alpha \, h_c^2$. Love's elastic solution of conical indentation provided relationships between the total and contact displacements and between the load and contact displacement:[26] $h = \beta h_c$ and $P = AE^* \cot \alpha/2$, where E^* is the plane–strain modulus $E^* = E/(1 - \nu^2)$, E is the Young's

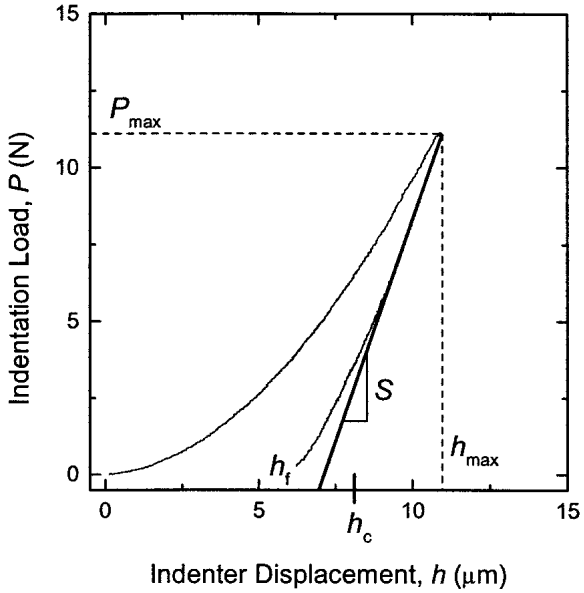

FIG. 1. Representative indentation load–displacement *P-h* trace of a typical ceramic (in this case, soda-lime glass). Parameters used in deconvoluting *P-h* traces to obtain material properties are indicated.

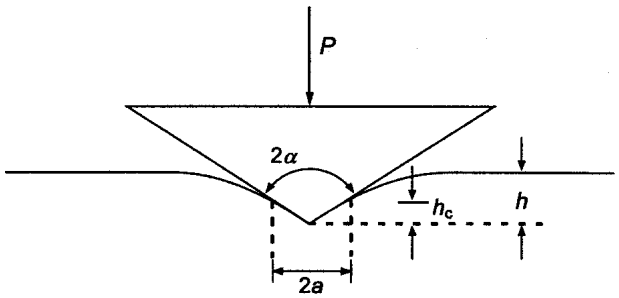

FIG. 2. Schematic cross section of the indentation process during loading of a ceramic material.

modulus, ν is Poisson's ratio, and $\beta = \pi/2$. These two expressions can be combined to yield the *P-h* relationship of a conical indenter:

$$P = \frac{\pi \tan \alpha}{2\beta^2} E^* h^2 \quad . \tag{2}$$

The elastic solution for indentation by a four-sided pyramidal (Vickers) indentation is identical to Eq. (2), except $\beta = 1.45$.[27] Plastic deformation during loading renders Eq. (2) invalid for most materials (except at exceptionally low loads), although $P \sim h^2$ for geometrically similar indenters.[28] Furthermore, Eq. (2) does not describe the *P-h* trace during a typical experiment because all indenter tips have some finite tip radius *R* and perhaps other imperfections that affect both the value of α and the quadratic relationship with contact depth shown above.[5]

In the absence of other, external, "independent" information (such as the yield stress) the unloading slope is the only unambiguous measure of the elastic contact stiffness $S = dP/dh$ (Fig. 1). The compliance $C = S^{-1}$ is related to the elastic modulus of the material being contacted by the following expression:[7]

$$E^* = \frac{\pi^{1/2}}{2CA^{1/2}} \quad . \tag{3}$$

Equation (3) is valid for indentation by an arbitrary axisymmetric indenter[29] regardless of the strain hardening properties of the material being indented or the presence of residual stresses.[30] The plane–strain modulus in Eq. (3) is often replaced by the so-called "reduced modulus" to account for elastic deformation of the indenter tip, where the reduced modulus is defined as[31]

$$E_r = \left(\frac{(1 - \nu^2)}{E} + \frac{(1 - \nu_i^2)}{E_i} \right)^{-1} \quad , \tag{4}$$

where E_i and ν_i are the elastic modulus and Poisson's ratio of the indenter, respectively (here taken to be 1141 GPa and 0.07 for diamond).[6] Equation (3) does not provide any information concerning the shape of the unloading curve, so the method used to determine dP/dh at peak load is a matter of some debate. If a specific type of curve is fit to some portion of the unloading data (such as a power-law curve), that curve can be related to the type of indenter. For instance, Doerner and Nix[32] used a straight-line fit to the upper 33% of the unloading curve, implying that the contact area did not change on initial unloading (similar to a flat punch). Oliver and Pharr[6] suggested a power-law curve with an exponent of 3/2, implying that the indenter tip was best approximated by a paraboloid of revolution:

$$P = k(h - h_f)^n \quad , \tag{5}$$

where, *k,* h_f, and *n* are fitted parameters (but on average *n* should be around 3/2). The stiffness is then obtained by analytic differentiation of Eq. (5). In the analysis here, Eq. (5) will be fit to some portion of the unloading curve to determine *S*.

The projected contact area at peak load *A* can be determined from the residual impression if the diagonals do not recover on unloading. It can also be determined from the *P-h* trace using the procedure outlined in Oliver and Pharr.[6] First the contact displacement is determined from the displacement at peak load h_{max} (Fig. 1):

$$h_c = h_{max} - \epsilon P_{max} C \quad , \tag{6}$$

where ϵ is a constant related to the form of the unloading trace, here taken to be 0.75 (corresponding to $n = 3/2$ for a paraboloid of revolution). Ideally, this contact displacement can be directly related to the projected contact area of the indenter tip purely by geometry. Due to the aforementioned imperfections in typical indenter tips, however, it is common to relate the area to the contact depth by some area function $A = f(h_c)$. There are many proposed forms of *f* in the nanoindentation literature with a variety of forms and with varying number of constants. Some are based on geometrical arguments,[8,33,34] others on experimental measurements of the tip radius,[35,36] while still others are almost completely empirical.[6,37,38] The area function of Thurn and Cook is used in this analysis because it specifically prescribes an effective tip radius R_{eff} and effective equivalent cone angle α_{eff} based on the calibration results and has the following form:[8]

$$A = \pi \tan^2 \alpha_{eff} h_c^2 + 4R_{eff} \pi h_c + 4R_{eff}^2 \pi \cot^2 \alpha_{eff} \quad . \tag{7}$$

An estimate of R_{eff} is important for understanding the shape of the *P-h* traces, especially at displacements on the order of R_{eff}. The parameter chosen here to represent the "lost" indentation volume due to tip truncation R_{eff} is also important for estimating the stress field and understanding the shape of the *P-h* traces, especially at displacements on the order of the tip truncation. The cone angle is important for estimating the stress field around the indenter and thus for comparing experimental results with finite element simulations and their resulting scaling laws.[39]

II. EXPERIMENTAL

The indentation apparatus used in this analysis is depicted schematically in Fig. 3. Load was transmitted to the sample via a sharp four-sided pyramidal (Vickers) diamond indenter tip located at the end of a loading shaft. The shaft was driven by a direct current (dc) servo micrometer so the indenter tip was nominally under displacement control. Displacements were imposed at rates

between 0.1 and 1 μm s^{-1}, although for stiff materials such as those examined here, the imposed displacement rate was significantly greater than the displacement rate of the tip. Load was measured with a 100-N resistance load cell in series with the indenter tip and displacement measured with capacitance gauges at two points to eliminate the effects of tilt in the loading shaft. The load and displacement resolutions were ±0.05 N and ±0.05 μm, respectively. The apparatus was designed to function in two separate modes: the first involved mounting the indenter atop an inverted microscope for *in situ* observation of the indentation event (on transparent materials) and the second involved clamping the sample to the base of the indenter (not shown) for precise displacement measurements during the contact event. In the second mode, the sample was clamped to the frame by gluing it to an aluminum sled that was then bolted to the floor of the indenter. The indentation apparatus is essentially the same machine described in Cook and Pharr[13] and used by Suresh *et al.*[18] As mentioned in Sec. I, many similar devices have been built privately and commercially to probe the elastic, plastic, viscous, and fracture properties of various materials (Refs. 2 and 9–20 allude to some of these devices). The nonmetal materials used in this analysis were chosen to cover a wide range of mechanical properties. Table I lists the materials examined with a short description of each.[40–51] All samples were polished to a mirror finish (1-μm diamond paste). The soda-lime glass, sapphire, and NaCl were all optically transparent and used for the *in situ* indentation observation experiments.

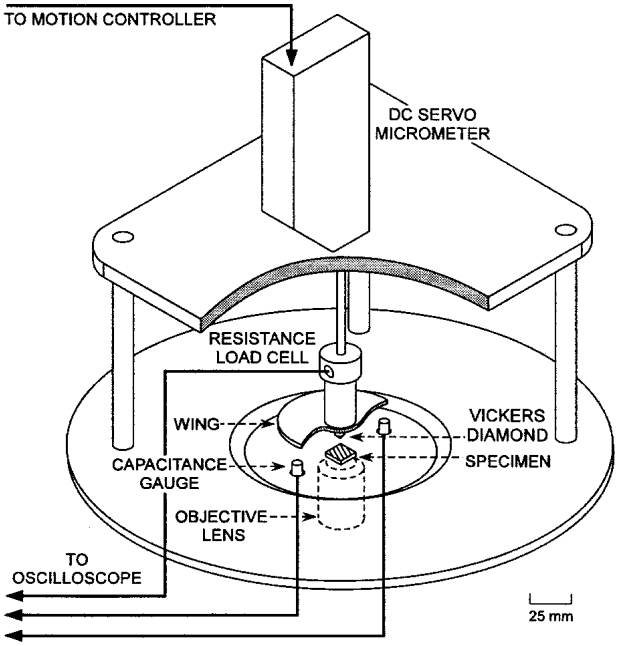

FIG. 3. Schematic diagram of the apparatus used here to perform depth-sensing indentation at macroscopic loads.

III. RESULTS

A. Sample clamping and column compliance

Macroscopic-scale DSI experiments were performed previously, but the effects of column compliance and sample clamping were sometimes ignored.[2,12] The effect of sample clamping can be seen in the *P-h* traces of Fig. 4 (on fused silica). The unclamped sample required considerably more displacement to support a given a load. Though not shown here, the moduli and hardness determined from the *P-h* curves of Fig. 4 using the Oliver and Pharr method outlined below differed by a factor of two (i.e., the unclamped sample showed values of modulus and hardness half the magnitude of the clamped and literature values).

The compliance of column C_f was determined by treating the indenter and sample as springs in series so that

$$C_t = C_f + C \quad , \tag{8}$$

where $C = S^{-1}$ is the sample compliance and C_t is the total measured compliance. The sample compliance was related to the projected contact area at peak load using

TABLE I. Summary of materials used in this study.

Material	Description	*E* (GPa)	*H* (GPa)	Reference(s)
Soda-lime glass	Commercial microscope slide	70	5.9	40, 13
Sapphire	99.995% Al_2O_3; (0001) single crystal	425[a]	21.8	41, 13
Silicon	(100) single crystal	169	9.6	42, 2
Al_2O_3–TiC	64/35 wt%, hot isostatically pressed	420	23.0	43, 44
$BaTiO_3$	Polycrystalline, capacitor grade	130[b]	5.9	45, 46
Synroc	Polycrystalline, titanate ceramic	189	10.3	46
Polycrystalline alumina	Surgical grade alumina	400	16.1	46
Y-stabilized tetragonal zirconia polycrystal	Annealed at 1300 °C	220[b]	17.8	47, 13
La_2O_3–Y_2O_3	9.1 mol% La_2O_3 polycrystalline	165	7.6	48
Fused silica	Optically flat substrate material	72	6.3	49, 13
NaCl	Commercial FTIR window, single crystal	50[b]	0.20	50, 51

[a]*c* axis.
[b]Voigt average from published elastic constants.

Eq. (3) and a plot of C_t versus $A^{-1/2}$ constructed from large indentations on soda-lime glass. Figure 5 shows *P-h* traces of two large indentations on soda-lime glass. The unloading slope *S* increases with increasing load, so *C* decreases with increasing load. The column compliance was obtained from Fig. 6, showing the total measured compliance (from *P-h* traces such as those shown in Fig. 5) against $A^{-1/2}$. The projected contact area *A* was determined by directly measuring optically the corner-to-corner area of the residual impressions for each indentation. The ordinate-intercept of a straight-line fit to the data in Fig. 6 provided an estimate of the column compliance $C_f = 0.021\ \mu m\ N^{-1}$. Clearly this is not a negligible contribution to the measured displacement, especially for large-load indentations on stiff materials such as alumina. During tip calibration, the column compliance is accounted for by replacing h_{max} with $h_{max} - P_{max}C_f$ and *C* with $C - C_f$ in Eqs. (3) and (6). Following calibration, it is simplest to subtract the PC_f product from the measured displacements prior to analysis of the *P-h* traces.

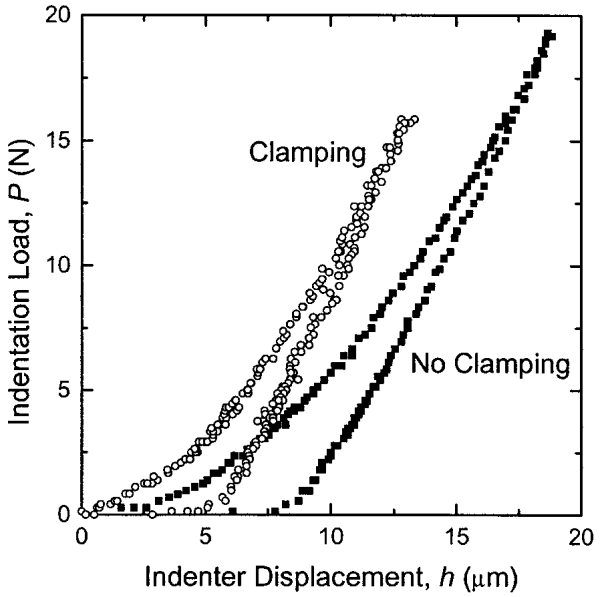

FIG. 4. *P-h* traces of fused silica with and without sample clamping. (Neither *P-h* trace has been corrected for column compliance.)

B. The projected contact area and the indenter area function

The abscissa of Fig. 6 was determined post-indentation by measurement of the residual indentation impression areas on soda-lime glass. In fact, this method of determining *A* will be used extensively in this analysis, so it is fitting to provide some experimental evidence for the implicit assumption being made here, that the impression diagonal 2*a* does not significantly recover on unloading. It is well known that the depth of the indentation impression recovers significantly on unloading.[23] It would seem plausible that the surface of the indentation, too, might elastically recover on unloading. The amount of elastic recovery of the diagonals during unloading on soda-lime glass, sapphire, and NaCl was examined by comparing the diagonal lengths measured during loading with those measured from the residual impression. Figure 7 shows *P-h* traces for indentations on all three

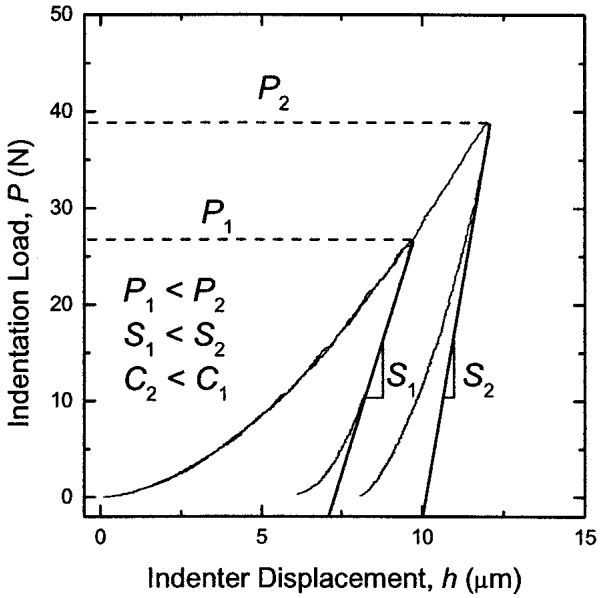

FIG. 5. *P-h* traces of large indentations on soda-lime glass showing the increase in contact stiffness *S* with increasing load *P*. (Both *P-h* traces have been corrected for column compliance.)

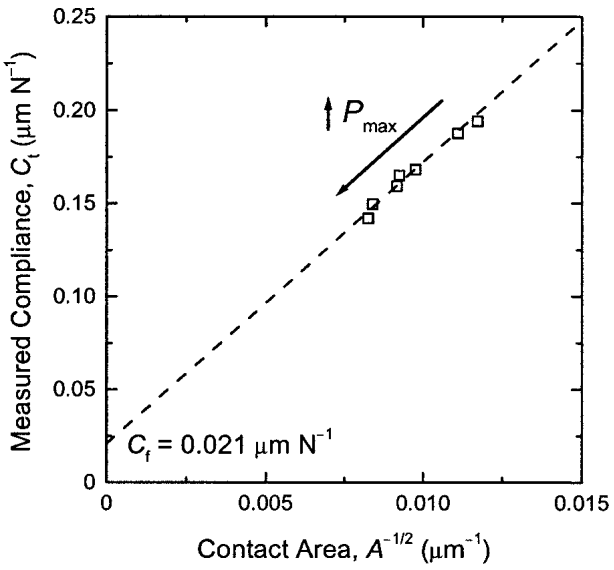

FIG. 6. Column compliance calibration plot: total measured compliance from the *P-h* data and projected contact area from measurements of the post-indentation residual impression (soda-lime glass).

materials. Indentations were performed over a wide range of loads on soda-lime glass [Fig. 7(a)] and sapphire [Fig. 7(b)]. The loading curves lie on top of one another and both materials show significant elastic recovery on unloading ($h_f < h_{max}$), as proposed above. Figure 7(c) shows multiple indentations on NaCl to peak loads near 4.5 N. For these indentations, the indenter was held at the peak imposed displacement for 30 s, resulting in the small amount of creep and relaxation seen near the peak where the load decreased and displacement increased with time. The unloading curve is nearly linear and $h_f \sim h_{max}$, indicating little elastic recovery in the depth of the impression on unloading.

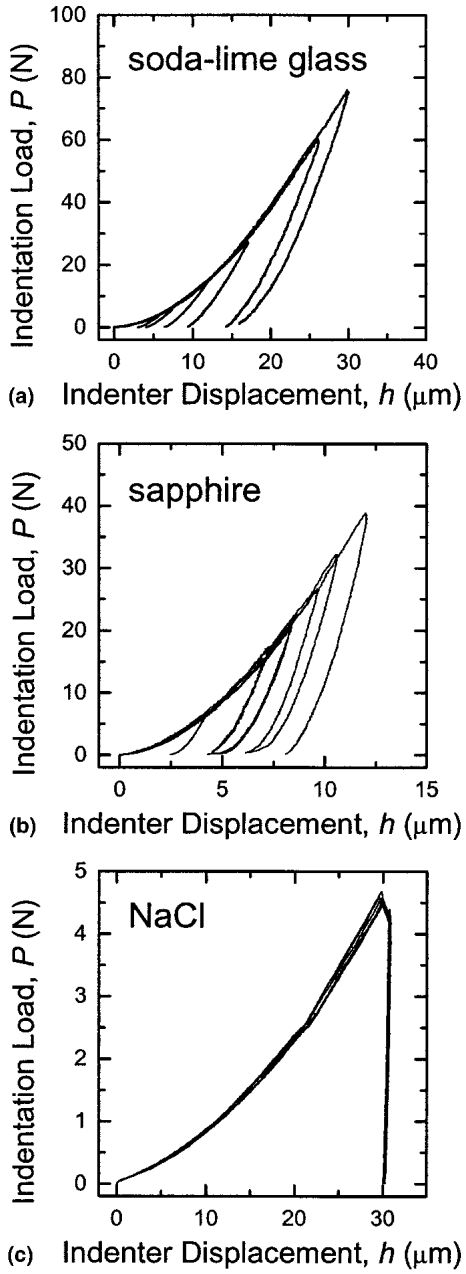

FIG. 7. *P-h* traces of indentations on (a) soda-lime glass, (b) sapphire, and (c) NaCl. The *P-h* traces have been corrected for column compliance.

Figure 8 compares the contact area during loading and the residual impression on these three materials. Figure 8(a) is an image of the contact area during loading of a soda-lime glass sample (from beneath the indenter tip, looking through the glass sample) at a load of 12.4 N and Fig. 8(b) is the residual impression of a 12 N indentation on the same sample. Shear faults can be observed directly outside the contact area (the dark area) in Fig. 8(a) as bright areas aligned along the contact. The residual impression in Fig. 8(b) is accompanied by radial and lateral cracking, which initiated during the early and late stages of unloading,[13] respectively. The length of the diagonals in Figs. 8(a) and 8(b) are the same $a \approx 33$ μm. Radial cracking during loading initiated at 42 N, but the length of the diagonals, though much more difficult to measure, remained the same as those measured from the residual impression. On sapphire, radial cracks initiated at 5 N during loading, as seen in Fig. 8(c), which shows the contact under a load of 8 N. The residual impression shown in Fig. 8(d) is from an 8.3-N indentation and has approximately the same diagonal length ($a \approx 16$ μm as opposed to 15 μm under a load of 8 N). The slight discrepancy between the values of the loads used for the *in situ* and residual impressions observed for soda-lime glass and sapphire are due to the displacement-control nature of the indenter. This discrepancy is rendered inconsequential by the quantitative analysis below. Finally, Figs. 8(e) and 8(f) show the contact on NaCl under a load of 4.3 N and the residual impression of an indentation to the same load. Again, the length of the diagonal is the same during loading, as they are following complete unload, in this case $a \approx 234$ μm. Though these materials cover a wide range of modulus and hardness (Table I), they all show negligible surface recovery of the diagonals during unloading.

The phenomenon of surface recovery for transparent materials was examined quantitatively as well. Figures 9(a)–9(c) show a comparison of the contact area measured during loading and post-indentation from the residual impression diagonals on soda-lime glass, sapphire, and NaCl, respectively, with increasing indentation load. The two estimates of area coincide within experimental uncertainty for all three materials (which span the entire range of E^* and H investigated in this study). Empirical linear fits to the *in situ* data [Eq. (2)] are indicated by solid lines. The onset of radial cracking on loading during indentation of soda-lime glass and sapphire is indicated by vertical dashed lines. Radial cracking during loading did not appear to significantly affect the linear *A-P* trend observed in Figs. 9(a) and 9(b) and predicted by geometric similarity.

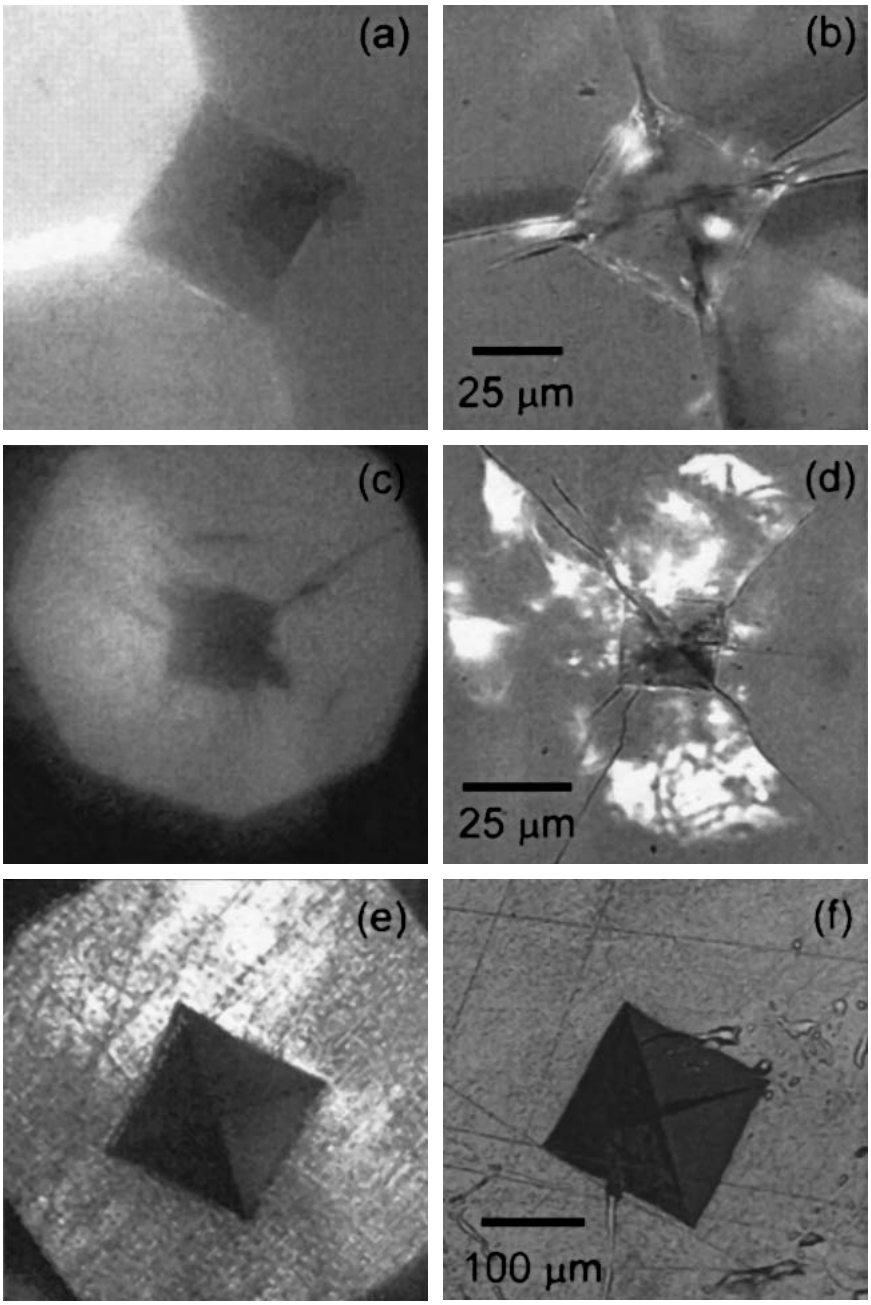

FIG. 8. Images of the contact region during loading (left) and following complete unload (right). (a) The contact region in soda-lime glass under 12.4 N load. (b) The residual impression of a 12 N indentation in soda-lime glass. (c) The contact region in sapphire under 8 N load (note the radial cracking). (d) The residual impression of an 8.3 N indentation in sapphire. (e) The contact region in NaCl under 4.3 N load. (f) The residual impression of a 4.3 N indentation in NaCl.

The area function, Eq. (7), was calibrated to determine the effective equivalent cone angle α_{eff} and effective tip radius R_{eff} using the procedure outlined in Oliver and Pharr[6] and Thurn and Cook.[8] Four materials were used in the calibration procedure: soda-lime glass, silicon, Al_2O_3–TiC, and sapphire (Table I). The area function fits the data well, following four iterations, over two orders of magnitude of contact depth, as shown in Fig. 10. The area function parameters obtained were $\alpha_{eff} = 70.40°$ and $R_{eff} = 3.30$ μm. The effective equivalent cone angle can be compared with the ideal equivalent cone angle of a Vickers indenter of 70.30°. The area calculated from the *P-h* curves and Eqs. (6) and (7) for a variety of ceramic materials (including the calibration materials) is compared with the corner-to-corner area measured post-indentation in Fig. 11. The agreement is excellent over three orders of magnitude of area. The area calculated in this manner also compares well to the area observed

during loading, as shown in Fig. 9. Note that the contact area at peak load is predicted well without using correction factors to Eq. (3) that would (i) account for the noncircular projected area shape of the Vickers indenter[52] and (ii) account for the horizontal displacements of material not considered in Sneddon's analysis.[53]

The area function, Eq. (7), was also used to calculate h_c from the area measured during loading (plotted in Fig. 9 for soda-lime glass, sapphire, and NaCl). These values of h_c were then compared to the measured total displacement h (minus the effect of column compliance) to obtain estimates of β ($= h/h_c$) during loading, as shown in Fig. 12 as a function of h. (The β values for $h < 2R_{eff}$ are probably inaccurate; area functions do not work well in this domain, rendering standard deconvolution methods uncertain.[8]) Shown on Fig. 12 as horizontal dashed lines are $\beta = \pi/2$ from Love's elastic solution for a cone,[26] $\beta = 0.91$ from experimental measurements of elastic recovery of Vickers indentation impressions,[23] and $\beta = 0.77$, which is a lower limit on β proposed by Marx and Balke based on elastic-plastic finite element simulations.[54] Several features of Fig. 12 are striking. First, β is an increasing function of h for all three

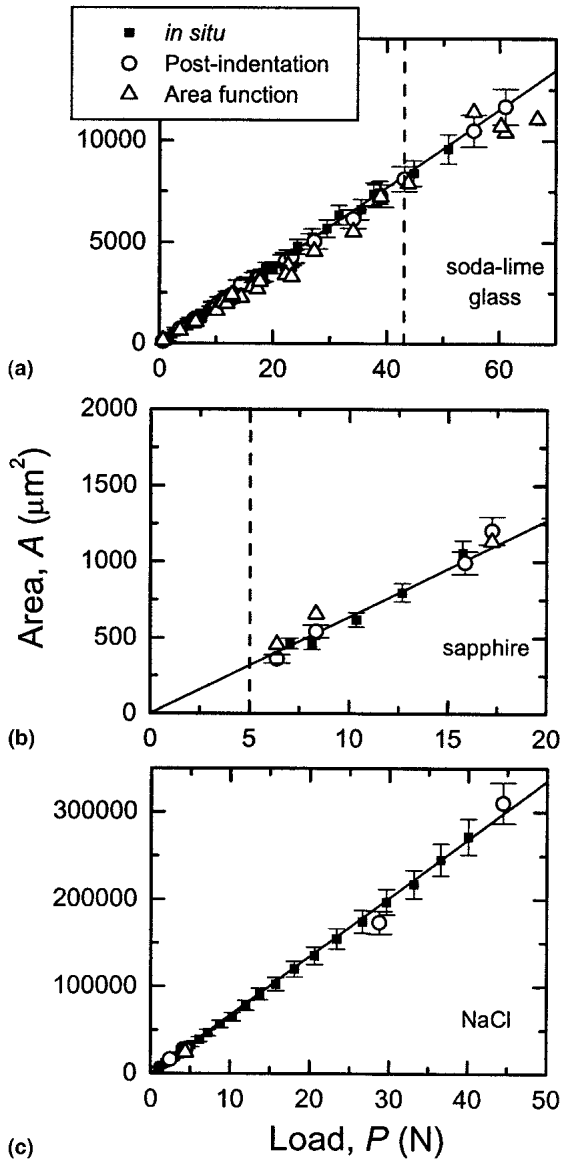

FIG. 9. Projected contact area measured *in situ,* post-indentation (corner-to-corner), and calculated from the *P-h* data with increasing load for (a) soda-lime glass, (b) sapphire, and (c) NaCl. The vertical dashed line denotes the threshold for radial cracking on loading. Solid lines are empirical linear fits to the *in situ* data [Eq. (2)].

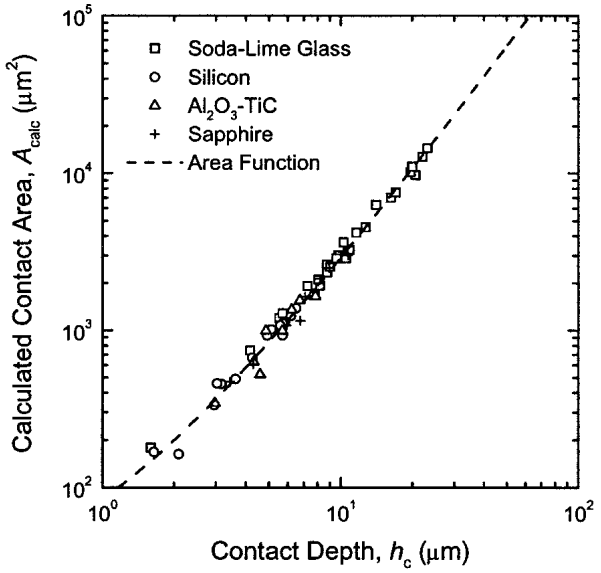

FIG. 10. Area function calibration plot: $\alpha_{eff} = 70.40°$ and $R_{eff} = 3.30$ μm used in Eq. (7).

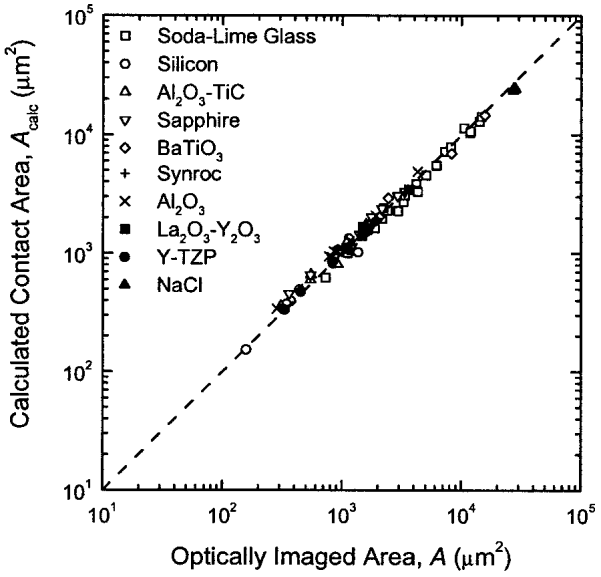

FIG. 11. Calculated contact area at peak load compared with the area measured from the residual indentation impressions on a variety of ceramic materials.

materials, although it levels off for $h > 20$ μm in NaCl. Second, β decreases with decreasing E (Table I) but is not an obvious function of E/H(E/H = 279 for NaCl, 22.9 for sapphire, and 11.7 for soda-lime glass, all based on experimental measurements shown in Sec. IV) On average, $\beta > 1$ as expected for soda-lime glass and sapphire (elastic sink-in). However, for the extremely ductile NaCl, $\beta < 1$, indicating pileup around the indenter during loading.

C. Modulus and hardness

The plane–strain modulus can be determined from Eqs. (3) and (4) if the unloading stiffness and projected area at peak load are known. Similarly, the hardness can be determined from Eq. (1). The area A can, in this case, be determined two different ways, as emphasized in Fig. 11. It can be measured following the indentation event or determined from Eqs. (6) and (7). The plane–strain modulus determined using the area function parameters given above is shown with contact depth for a variety of ceramics in Fig. 13(a). The average moduli agree with the accepted values for most materials (see below) and are nearly independent of contact depth. The data for barium titanate and soda-lime glass appear to have slight trends of decreasing E^* with increasing h_c; possibly due to the fact that the frame compliance was determined from the average response of four different materials. Similarly, the hardness obtained from the area function is shown in Fig. 13(b). Again, most of the measured hardness values are in agreement with the literature values and are independent of contact depth. The literature modulus and hardness values used for comparison were obtained from the references listed in Table I. Hardness and moduli determined using the corner-to-corner area from the residual indentation impressions following the indentation event were identical, within experimental error, to those shown in Figs. 13(a) and 13(b), as may be confirmed from the area comparison shown in Fig. 11. The measured modulus and hardness are compared with the literature values shown in Table I in Figs. 14(a) and 14(b), respectively. Both the measured modulus and hardness are lower than the literature values for sapphire and polycrystalline alumina, with deviations between 15% and 30%. However, this high deviation was not seen in an equally stiff and hard material, Al_2O_3–TiC, which, like most of the materials, deviated 10% or less from the literature values (using an assumed Poisson's

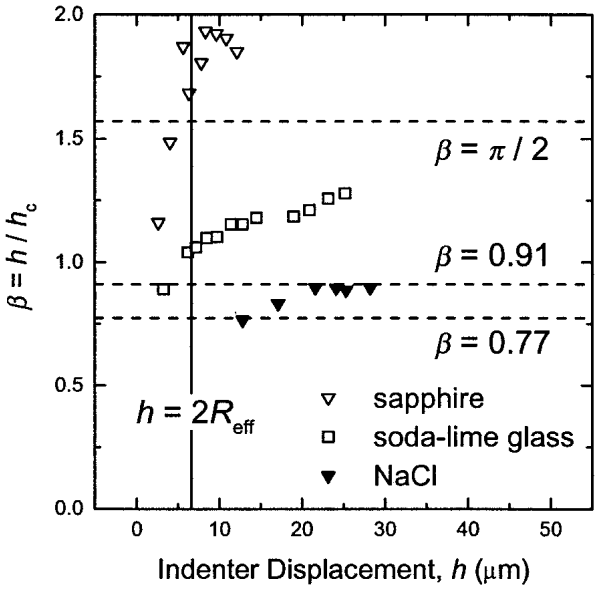

FIG. 12. Evolution of $\beta(=h/h_c)$ during loading of soda-lime glass, sapphire, and NaCl. The elastic solution ($\beta = \pi/2$),[26] a proposed lower limit ($\beta = 0.77$),[54] and an experimentally obtained value of $\beta(= 0.91)$[23] are also shown as horizontal dashed lines. The data for $h < 2R_{eff}$ (solid vertical line) are probably inaccurate.[8]

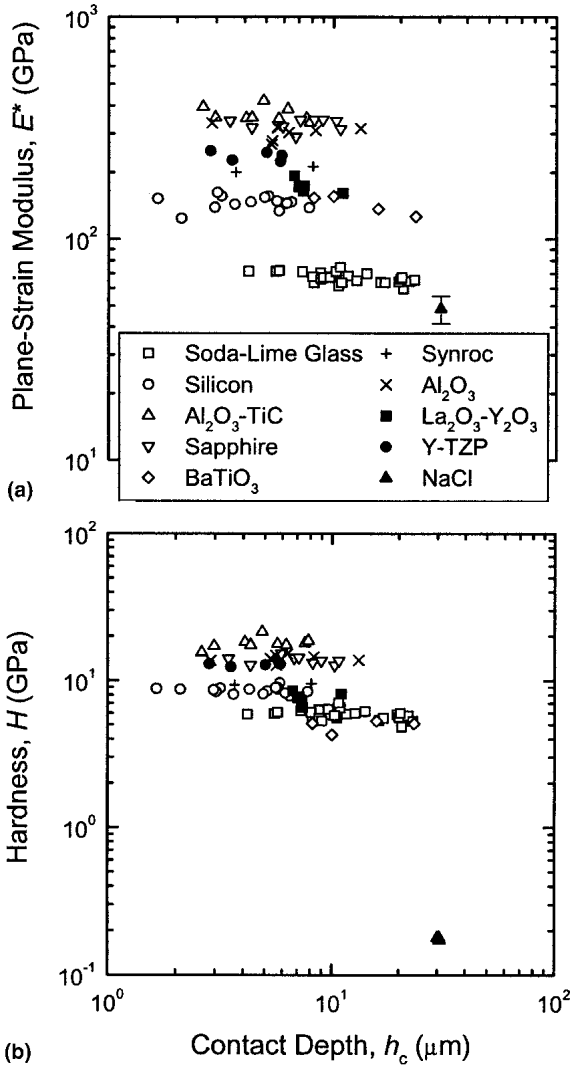

FIG. 13. (a) Plane–strain modulus determined using the area function with contact depth for a variety of ceramics. (b) Hardness determined using the area function with contact depth for a variety of ceramics.

ratio to convert E^* to E). In particular, the modulus and hardness calculated for NaCl were in close agreement with the literature values despite the effects of pileup observed during the *in situ* experiments.

IV. DISCUSSION

The calibration method of Oliver and Pharr, designed for analysis of nanoindentation *P-h* data, can readily be applied to macroscopic-scale indentation analysis. Utilizing the method of Oliver and Pharr for extraction of mechanical properties has the additional advantage of identifying the effective properties of the indenter tip via a two-parameter area function. The tip here was found to have an effective tip radius of 3.30 μm. This finite tip radius had a drastic effect on the loading portion of the load–displacement trace. Figure 15 displays the loading and unloading curves for a 13 N indent on soda-lime glass on logarithmic scales. The abscissa h is h for the loading data and $h - h_f$ for the unloading data (where h_f was determined directly from the *P-h* data). The solid line overlapping the loading data is a line of slope two, indicating perfect quadratic loading. This line begins to deviate from the data below about h = 7.5 μm, about twice the effective tip radius. The deviation is highlighted in Fig. 15 by a dashed vertical line at $h = 2R_{eff}$. It has been shown that *P-h* traces in the elastic limit at very small displacements can be quantified by either describing the indenter as a sphere of radius R or as a blunted conical indenter of tip radius.[5,55,56] Theoretical investigations of tip-blunting (or tip-rounding) have shown that the entire *P-h* trace is modified by the presence of a finite tip radius and not just the small-displacement region of the *P-h* trace where the indenter is approximately spherical.[33–34,57,58] Cheng and Cheng[59] suggested that the loading curve is best described by a second-order polynomial and used such fits to describe finite element results for conical indentation. The dashed line in Fig. 15 is an empirical second-order polynomial fit to the loading data and describes it well over the entire range of h. Modifications have been made to the quadratic *P-h* relationship on loading [Eq. (2)] accounting for both the elastic–plastic nature of loading and the effects of tip radius.[60]

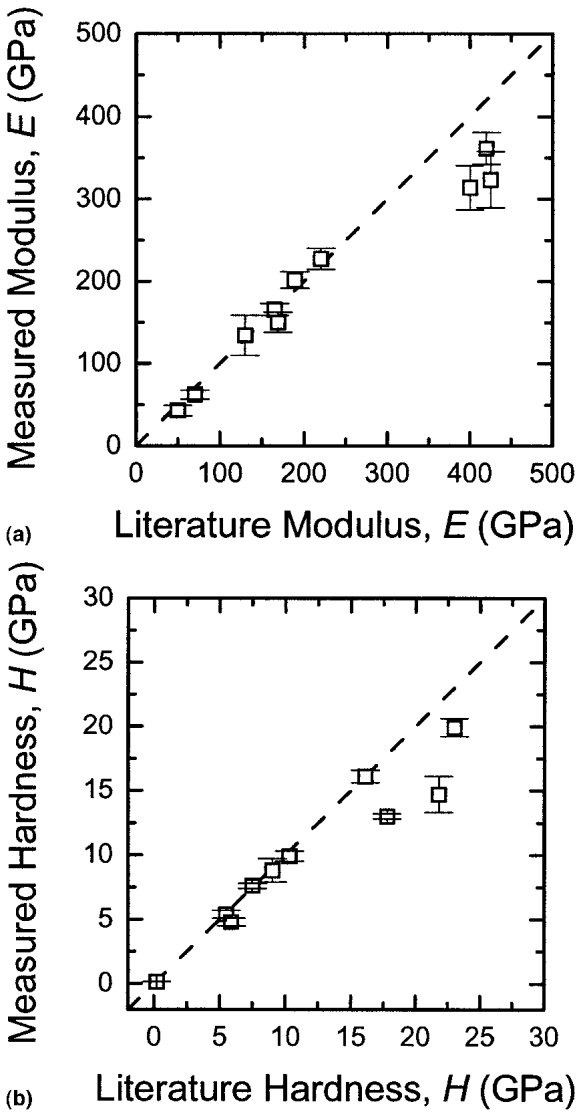

FIG. 14. Measured (a) modulus and (b) hardness compared with the literature values. Assumed Poisson's ratios are as follows: 0.17 for soda-lime glass, 0.06 for Si,[40] and 0.2 for all others.

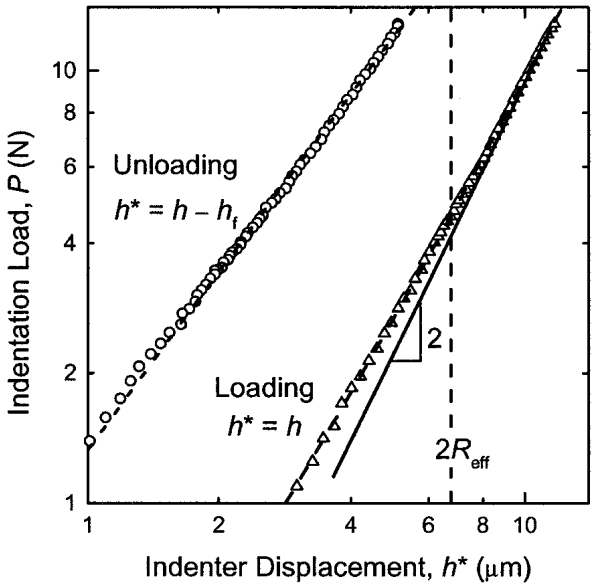

FIG. 15. *P-h* curve for a 13 N indentation on soda-lime glass in logarithmic coordinates. $h^* = h$ for the loading curve and $h^* = h - h_f$ for the unloading curve. The solid line of slope two is representative of perfect quadratic loading while the dashed line is a second-order polynomial fit to the loading curve. The vertical dashed line is at $h = 2R_{eff}$. The dotted line is a straight-line fit to the unloading data. (The *P-h* data have been corrected for the effects of column compliance.)

A straight-line fit of the unloading data (in the logarithmic coordinates) in Fig. 15 resulted in a power-law dependence of $n = 1.37$ and is shown as a dotted line. However, when a nonlinear curve fit was performed using Eq. (5) on the original load–displacement unloading data (also corrected for column compliance), a power-law dependence of $n = 1.53$ was obtained, as suggested by the experimental *P-h* data of Oliver and Pharr.[6] The straight-line fit to the unloading data on logarithmic axes was weighted more strongly by the data near $h^* = 0$, where identification of A is critical, and the nonlinear fit was weighted more strongly by the data near the peak load and displacement—the region of the *P-h* curve used to deduce the stiffness. The data of Fig. 15 then support the idea that a nonlinear power-law fit to experimental data on linear axes is recommended because it weights the data near the peak load and displacement and provides a greater degree of flexibility by allowing h_f to vary.

The unloading curve was also more susceptible to column compliance effects than the loading curve. Figure 16 is a logarithmic plot of the loading and unloading data for a 31 N indentation on Al_2O_3–TiC. The solid data points are the raw data and the open data points have been corrected for column compliance. The abscissa label h^* is as defined above for Fig. 15. Both the raw and compliance-corrected loading data appeared quadratic for $h > 2R_{eff}$, as in Fig. 15. The raw and corrected unloading data, however, had different power dependencies. When a nonlinear curve fit was performed using Eq. (5) the power dependencies were n = 1.45 and n = 1.59 for the raw and corrected data, respectively. The calculated modulus and hardness values were increased by 28% and 5%, respectively, on correcting the raw *P-h* data for column compliance.

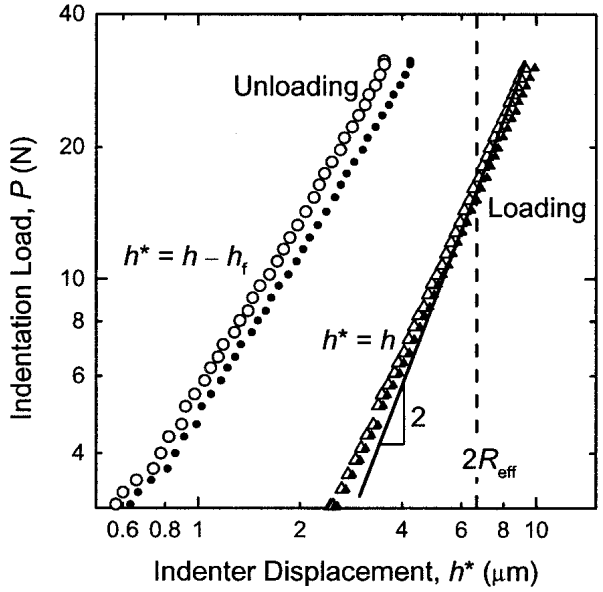

FIG. 16. *P-h* curve for a 31 N indentation on Al_2O_3–TiC in logarithmic coordinates. The abscissa is as defined in Fig. 15. The open symbols have been corrected for the effects of column compliance, and the solid symbols have not.

V. CONCLUSIONS

DSI at macroscopic loads was performed on a set of ceramic materials encompassing a wide range of modulus *E,* hardness *H,* and *E*/*H* values. The custom-built indenter allowed continuous load–displacement, *P-h*, measurements to be made during Vickers indentation at loads up to 100 N. The macroscopic scale of the indentations, along with the capability of the instrument to be mounted on top of an inverted optical microscope, allowed direct verification of the invariance of contact-diagonal lengths at their peak–load values during indentation unloading, an assumption implicit in post-indentation estimation of hardness from residual impression dimensions. Optical measurement of the residual impression dimensions and associated contact areas also enabled a simple implementation of the Oliver–Pharr[6] iteration scheme for simultaneous calibration of indenter frame compliance and indenter tip shape. This scheme, based on Sneddon's analysis[7] of the relationship between modulus, contact stiffness and projected contact area was then used to extract *E* and *H* estimates directly from the unloading *P-h* traces, without direct reference to observations of impression dimensions, in much the same manner as "nanoindentation" tests. The estimated values were found to be in agreement with independent measurements and the importance of adequate specimen clamping and frame compliance correction, along with knowledge of the analytically applicable displacement range set by the tip shape in obtaining this agreement were all highlighted. In particular, a two-parameter area function was used here for the tip, providing an estimate of the effective tip radius (about 3.3 μm for the commercial Vickers diamond used); indentation displacements smaller than about twice the tip radius were observed to violate the quadratic loading response associated with geometrically similar contacts.

Applications of macroscopic DSI beyond estimations of *E* and *H* for homogeneous ceramics are vast, and some were identified here. Quadratic loading was observed at large displacements and *in situ* observations revealed that it was maintained in materials that exhibited radial cracking during indentation contact. Direct observation of the contact impressions combined with *P-h* measurements also allowed the parameter β, the total:contact depth ratio, to be measured, revealing a range of β values associated with material-dependent indentation plasticity.

Instrumented indenters for DSI at macroscopic loads are easy to build and use and can thus be customized easily for specific applications. The only qualifications,

as shown here, are that (for indentation of stiff ceramic materials) the samples must be securely clamped in place and the indenter must be calibrated to account for compliance of the loading shaft. The simplicity of the system allows attention to be focused on contact phenomena and materials characterization and not on the instrumentation itself. Thus the technique is ideally suited for examining the effects of different indenter shapes and materials, rough surfaces, viscous contacts, adhesive contacts, thick films, and porous materials without worrying about artifacts introduced by feedback loops or extremely small-scale instrumentation.

ACKNOWLEDGMENTS

The authors wish to thank Yvete Toivola and Matthew Cunningham for helpful discussions. Supplemental financial support for Jeremy Thurn was provided by the Coating Process Fundamentals Program through the University of Minnesota Industrial Partnership for Research in Interfacial and Materials Engineering (IPRIME).

REFERENCES

1. J.B. Pethica, R. Hutchings, and W.C. Oliver, Philos. Mag. A **48,** 593 (1983).
2. R.F. Cook and G.M. Pharr, J. Hard Mater. **5,** 179 (1994).
3. B.J. Briscoe, K.S. Sebastian, and S.K. Sinha, Philos. Mag. A **74,** 1159 (1996).
4. J. Menčik, D. Munz, E. Quandt, E.R. Weppelmann, and M.V. Swain, J. Mater. Res. **12,** 2475 (1997).
5. T.F. Page, W.C. Oliver, and C.J. McHargue, J. Mater. Res. **7,** 450 (1992).
6. W.C. Oliver and G.M. Pharr, J. Mater. Res. **7,** 1564 (1992).
7. I.N. Sneddon, Int. J. Engng. Sci. **3,** 47 (1965).
8. J. Thurn and R.F. Cook, J. Mater. Res. **17,** 1143 (2002).
9. F. Fröhlich, P. Grau, and W. Grellmann, Phys. Status Solidi (a) **42,** 79 (1977).
10. J.L. Loubet, J.M. Georges, D. Marchesini, and G. Meille, J. Tribol. **106,** 43 (1984).
11. J.E. Ritter, T.J. Lardner, L. Rosenfeld, and M.R. Lin, J. Appl. Phys. **66,** 3626 (1989).
12. G.M. Pharr and R.F. Cook, J. Mater. Res. **5,** 847 (1990).
13. R.F. Cook and G.M. Pharr, J. Am. Ceram. Soc. **73,** 787 (1990).
14. W. Mason, P.F. Johnson, and J.R. Varner, J. Mater. Res. **7,** 3112 (1992).
15. M. Sakai, Acta Metall. Mater. **41,** 1751 (1993).
16. B.J. Briscoe and K.S. Sebastian, Proc. R. Soc. Lond. A **452,** 439 (1996).
17. J. Gubicza, A. Juhász, P. Tasnádi, P. Arató, and G. Vörös, J. Mater. Sci. **31,** 3109 (1996).
18. S. Suresh, J. Alcalá, and A.E. Giannakopoulos, MIT Case No. 7280, Technology Licensing Office, Massachusetts Institute of Technology, Cambridge, MA, U.S. Patent filed 1996.
19. J. Alcalá, A.E. Giannakopoulos, and S. Suresh, J. Mater. Res. **13,** 1390 (1998).
20. H. Öberg, P-L. Larsson, and O. Magnius, J. Test. Eval. **29,** 50 (2001).
21. B.R. Lawn, A.G. Evans, and D.B. Marshall, J. Am. Ceram. Soc. **63,** 574 (1980).
22. D.B. Marshall and A.G. Evans, J. Appl. Phys. **56,** 2632 (1984).
23. B.R. Lawn and V.R. Howes, J. Mater. Sci. **16,** 2745 (1981).
24. D.B. Marshall, T. Noma, and A.G. Evans, J. Am. Ceram. Soc. **65,** C175 (1982).
25. R.F. Cook, J. Am. Ceram. Soc. **77,** 1263 (1994).
26. A.E.H. Love, Quarterly Journal of Mathematics **10,** (1939).
27. G.G. Bilodeau, J. Appl. Mech. **59,** 519 (1992).
28. D. Tabor, *The Hardness of Metals* (Clarendon Press, Oxford, U.K., 1951), pp. 8–11, 112–113.
29. G.M. Pharr, W.C. Oliver, and F.R. Brotzen, J. Mater. Res. **7,** 613 (1992).
30. C-M. Cheng and Y-T. Cheng, Appl. Phys. Lett. **71,** 2326 (1997).
31. N.A. Stilwell and D. Tabor, Phys. Proc. Soc. Lond. **78,** 169 (1961).
32. M.F. Doerner and W.D. Nix, J. Mater. Res. **1,** 601 (1986).
33. C.W. Shih, M. Yang, and J.C.M. Li, J. Mater. Res. **6,** 2623 (1991).
34. H. Pelletier, J. Krier, A. Cornet, and P. Mille, Thin Solid Films **379,** 147 (2000).
35. S. Enders, P. Grau, and H.M. Hawthorne, in *Fundamentals of nanoindentation and Nanotribology II,* edited by S.P. Baker, R.F. Cook, S.G. Corcoran, and N.R. Moody (Mater. Res. Soc. Symp. Proc. **649,** Warrendale, PA, 2001), p. Q3.6.1.
36. J.M. Antunes, A. Cavaleiro, L.F. Menezes, M.I. Simões, and J.V. Fernandes, Surf. Coat. Technol. **149,** 27 (2002).
37. L.E. Seitzman, J. Mater. Res. **13,** 2936 (1998).
38. K. Herrmann, N.M. Jennett, W. Wegener, J. Meneve, K. Hasche, and R. Seemann, Thin Solid Films **377–378,** 394 (2000).
39. Y-T. Cheng and C-M. Cheng, Appl. Phys. Lett. **73,** 614 (1998).
40. G.R. Anstis, P. Chantikul, B.R. Lawn, and D.B. Marshall, J. Am. Ceram. Soc. **64,** 533 (1981).
41. J.B. Wachtman, Jr., W.E. Tefft, D.G. Lam, Jr., and R.P. Stinchfield, J. Res. Natl. Bur. Stand. Sect. A: Phys. Chem. **64,** 213 (1960).
42. W.A. Brantley, J. Appl. Phys. **44,** 534 (1973).
43. Product Bulletin, Minnesota Mining and Manufacturing Company (St. Paul, MN, 1987).
44. A. Goldstein and A. Singurindi, J. Am. Ceram. Soc. **83,** 1530 (2000).
45. D. Berlincourt and H. Jaffe, Phys. Rev. **111,** 143 (1958).
46. R.F. Cook, Ph.D. Thesis, School of Physics, University of New South Wales, Sydney, Australia (1985).
47. R.P. Ingel and D. Lewis, J. Am. Ceram. Soc. **71,** 265 (1988).
48. R.F. Cook, E.G. Liniger, and M.R. Pascucci, J. Hard Mater. **5,** 191 (1994).
49. S.M. Wiederhorn, J. Am. Ceram. Soc. **562,** 99 (1969).
50. M.A. Meyers and K.K. Chawla, *Mechanical Behavior of Materials* (Prentice-Hall, Upper Saddle River, NJ, 1999), p. 92.
51. C.A. Brookes, J.B. O'Neill, and B.A. Redfern, Proc. Roy. Soc. London Ser. A **322,** 73 (1971).
52. R.B. King, Int. J. Solids Structures **23,** 1657 (1987).
53. J.C. Hay, A. Bolshakov, and G.M. Pharr, J. Mater. Res. **14,** 2296 (1999).
54. V. Marx and H. Balke, Acta Mater. **45,** 3791 (1997).
55. A. Shimamoto, K. Tanaka, Y. Akliyama, and H. Yoshizaki, Philos. Mag. A **74,** 1097 (1996).
56. K. Zeng and C-H. Chiu, Acta Mater. **49,** 3539 (2001).
57. Y. Sun, T. Bell, and S. Zheng, Thin Solid Films **258,** 198 (1995).
58. Y. Sun, S. Zheng, T. Bell, and J. Smith, Philos. Mag. Lett. **79,** 649 (1999).
59. Y-T. Cheng and C-M. Cheng, J. Mater. Res. **13,** 1059 (1998).
60. J. Malzbender and G. de With, J. Mater. Res. **17,** 502 (2002).